Chapter 4

Bursty Langmuir Waves in the Cusp: TRICE

4.1 Introduction

The electron-beam plasma interaction in the Earth's auroral ionosphere produces a variety of plasma waves, and Langmuir waves are among the most intense and ubiquitous of these. Sounding rocket observations of Langmuir waves in both the night- and dayside aurora show similar features: the waves occur in bursts with durations from ms to hundreds of ms and amplitudes from mV/m to hundreds of mV/m (*Boehm* 1987; *McFadden et al.* 1986; *McAdams et al.* 1999). The bursts are modulated at frequencies ranging from < 1 kHz to > 50 kHz (*Ergun et al.* 1991; *Bonnell et al.* 1997; *LaBelle et al.* 2010). Satellite data confirm many of these observations (*Gurnett et al.* 1981; *Beghin et al.* 1981; *Stasiewicz et al.* 1996; *Kintner et al.* 1996; *Malaspina and Ergun* 2008).

The modulation of auroral Langmuir waves has been attributed to mixing of multiple wave normal modes on the Langmuir surface. Indeed, spectra of the modulated waves show multiple peaks, extremely well resolved in recent experiments (*LaBelle et al.* 2010). Linear (*Maggs* 1976; *Newman et al.* 1994b) and nonlinear (*Newman et al.* 1994a) theory suggests that the auroral electron beam can excite a range of Langmuir modes, including modes at oblique angles. There is some controversy, however, about the origin of the interfering waves. Most papers in the literature favor wave-wave interaction, whereby a primary Langmuir wave, directly excited by the beam, decays into a second Langmuir wave and a whistler or ion sound wave, with the observed modulation resulting from the beating of the two Langmuir waves (*Bonnell et al.* 1997; *Stasiewicz et al.* 1996; *Lizunov et al.* 2001; *Khotyaintsev et al.* 2001). The absence of evidence for the low frequency wave in many observations is explained by strong wave damping. An alternative hypothesis holds that two different Langmuir waves directly excited by linear processes at slightly different locations in the strongly inhomogeneous plasma mix to make the observed modulations (*LaBelle et al.* 2010). In this case, no third wave would be expected to occur.

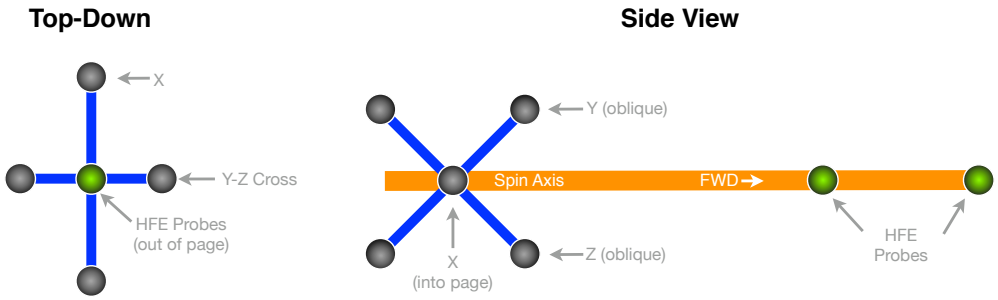

Figure 4.1: Boom and sensor elements of the two complimentary HF electric field experiments flown on the TRICE sounding rockets.

A significant shortcoming of previous rocket experiments lies in the absence of three-dimensional field data at high frequencies. Recently, however, the availability of higher rocket telemetry rates and the increasing power of onboard processing enabled the TRICE sounding rocket mission to include such measurements. In principle, having all three components of the electric field provides more information about the wave modes comprising the modulated Langmuir waves. Section 4.2 below describes the TRICE instrumentation; Section 4.3 shows measured three-dimensional waveforms; and Section 4.4 presents a model for explaining observed effects. Finally, Section 4.5 expands upon an ambiguity in the model.

4.2 Instrumentation

The Twin Rockets to Investigate Cusp Electrodynamics (TRICE) were launched 10 Dec 2007 at 0900 and 0902 UT, from Andoya, Norway, reaching apogees of 1145 km and 750 km. The rockets were launched into an active cusp, with poleward-moving auroral forms monitored with all-sky cameras and multiple radars. K_p was relatively low, with a value of two. The payload's spin axis was kept aligned with the background magnetic field, $\boldsymbol{B}_0$, by a NASA Attitude Control System (ACS), which activated at specific times during the flight, and was otherwise turned off to minimize interference. Each rocket carried electron and ion detectors, swept Langmuir probes, low-frequency to DC electric-field probes, magnetometers, and two complementary high-frequency electric-field instruments: the Dartmouth High-Frequency Electric-field experiment (HFE), and the NASA GSFC Tri-Axial Electric-Field Wave Detector (TAEFWD). Figure 4.1 shows the probe configuration for the HF instruments.

The Dartmouth HFE detects the potential difference between two 2.5 cm spherical probes, separated by 30 cm along the payload's spin axis. This ΔV signal provides an estimate of the the axial component of the electric-field, which is mainly parallel to the ambient magnetic field, given the payload alignment. The signal is band-pass filtered to the 100 kHz to 5 MHz band, and regulated by an Automatic Gain Control (AGC) system to enhance the dynamic range. The AGC control signal is sampled onboard at 20 kHz and telemetered with

other digital data. The regulated HF signal directly modulates a 5 MHz-bandwidth S-band transmitter, and the resulting waveform is continuously digitized at the ground telemetry station at 10 MHz, with 12-bit resolution. This instrument is the latest iteration of a design which has flown on numerous rocket campaigns in both $\boldsymbol{E}_{\parallel}$ and $\boldsymbol{E}_{\perp}$ configurations, including HIBAR (*Samara et al.* 2004), PHAZE II (*McAdams et al.* 1998), SIERRA, RACE (*Samara and LaBelle* 2006), ACES (*Kaeppler et al.* 2011), and CHARM II (*Kletzing et al.* 2012).

The GSFC TAEFWD measures ΔV between three pairs of 2.5 cm probes separated by 47.5 cm (X axis) or 45.5 cm (Y and Z axes) along three orthogonal axes: an X axis perpendicular to the payload spin axis, and Y and Z axes 45 degrees off of the spin axis, in a plane perpendicular to X. After filtering to a 4 MHz bandwidth (-3dB bandwidth), the onboard TAEFWD receiver synchronously digitizes these three signals, as well as the Dartmouth HFE output signal, at 8 MSps, in 2048-sample snapshots, with the snapshots being gathered at 15.625 Hz cadence, yielding a 0.4% duty cycle and a 1.92 MBps data stream (after packing into 10-bit words). The sensitivity level was approximately 80 μV/m, suitable for measurement of large-amplitude Langmuir waves in the cusp region.

Both payloads were affected by various payload systems failures and instrumental anomalies, resulting in the complete loss of particle data and interference in other data, including the generation of extraneous signals; however, the DC magnetometer and both HF electric-field experiments obtained good data over most of the flight. The HFE data in particular resulted in a study of cusp Langmuir waves (*LaBelle et al.* 2010).

Between ACS activations, imperfections in the payload weight distribution caused the payload to begin to misalign from $\boldsymbol{B}_0$, with the spin axis precessing around $\boldsymbol{B}_0$ by an increasing angle—an effect known as 'coning'. On TRICE, unlike most flights, this effect could not be compensated for because the payload attitude data provided by the ACS package was of low quality due to interference. Over the interval important to this study, the payload magnetometer showed a variance in $\boldsymbol{B}_0$ from perfect spin-axis alignment of 5-10%, implying a similar variance in the components of the electric field parallel and perpendicular to $\boldsymbol{B}_0$.

4.3 Observations

As shown by *LaBelle et al.* (2010), the TRICE high-flyer passed through auroral activity that generated significant high-frequency waves. Figure 4.2a is a 0 to 2.5 MHz spectrogram of HFE data from almost the entire flight (100 to 1100 seconds after launch). General features of this plot include: a 100 kHz rolloff due to the band-pass filter; vertical bands which are caused by the AGC system raising and lowering the noise floor when the total signal amplitude changes; additional, cadenced vertical bands at 60 s intervals, which are instrument-calibration signals injected into the receiver; and multiple horizontal bands, the strongest of which are due to interference from payload systems. Malfunctions in the particle instruments also resulted in periods of strong interference 100–400 kHz, e.g. at 710–845 s, 865–880 s, and 900–920 s. These broadly resemble natural auroral hiss, but have been attributed to arcing in high-voltage components (*LaBelle et al.* 2010).

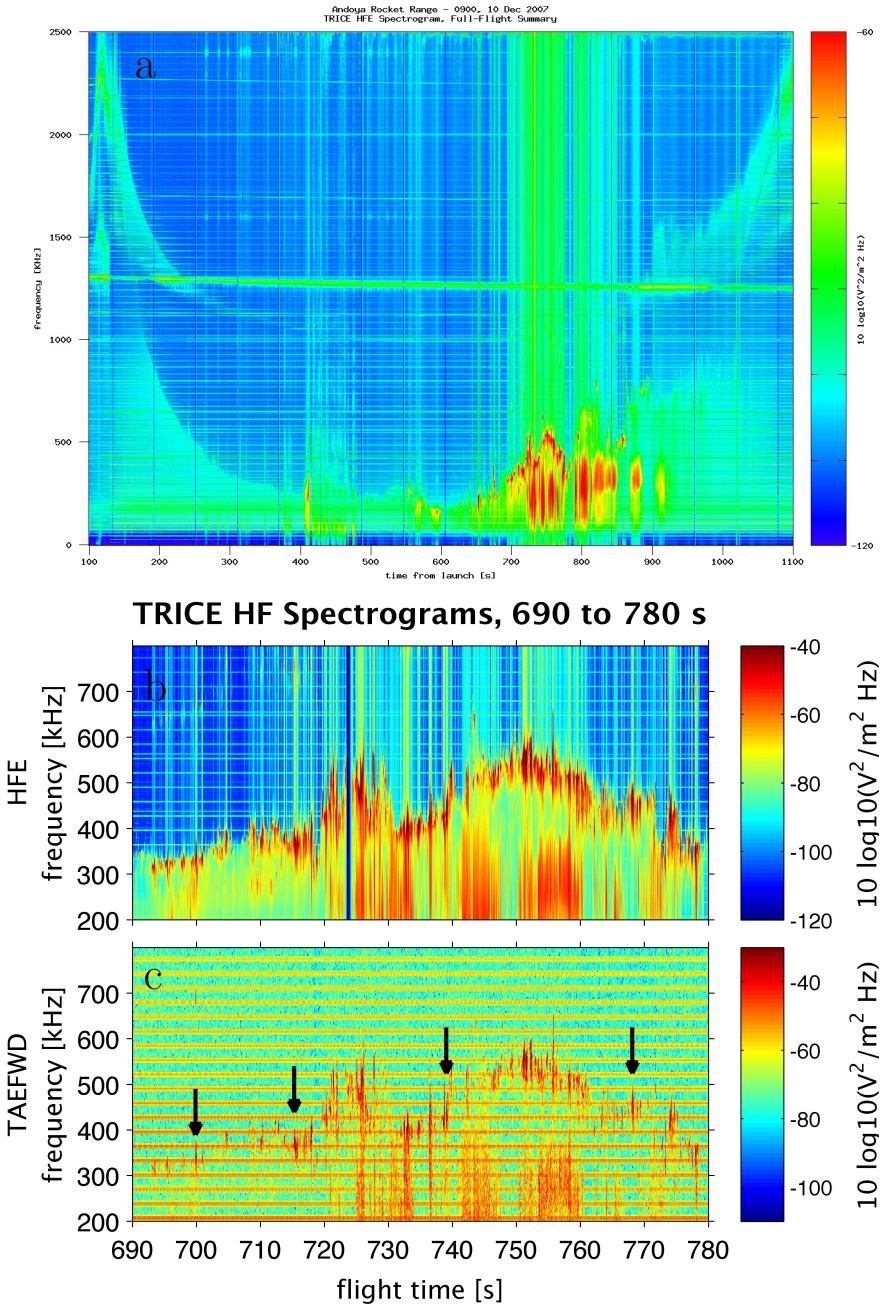

Figure 4.2: Spectrograms of TRICE HF electric field data. **a** shows a summary of the full flight covering 100 kHz–2.5 MHz and 100–1100 s, while **b** and **c** are HFE and TAEFWD Z' data covering a 200-800 kHz band from 690 to 780 s, the period of intense activity outlined in white in **a**. Black arrows in **c** indicate times of TAEFWD waveform snapshots examined in detail.

Besides the artificial features, the full-flight spectrogram shows signals of natural origin, such as wave cutoffs of the type which have proven effective for measuring electron plasma density on previous flights. Two such upper cutoffs can be seen near the beginning of this flight: a higher-frequency cutoff that emerges from diffuse noise near 2.5 MHz at 150 s and descends to around 1.2 MHz by 300 s, and a lower-frequency cutoff which is at 750 kHz at 200 s, 200 kHz at 400 s, and remains reasonably well-defined through most of the flight. This lower-frequency cutoff is interpreted as f_{pe}, which is an upper bound for the whistler mode during the portion of the flight when $f_{pe} < f_{ce}$, approximately 190 to 900 s. The upper cutoff is identified as the upper-hybrid frequency $f_{uh} = \sqrt{f_{pe}^2 + f_{ce}^2}$, given that f_{ce} is approximately 1.2 MHz throughout the flight. The relation between the frequencies of these cutoffs when they occur together lends confidence to their interpretations as f_{pe} and f_{ce}.

The second half of the flight includes lengthy periods of intense wave activity near the f_{pe} cutoff, and close inspection of waveforms shows that these consist of many bursts of Langmuir waves. *LaBelle et al.* (2010) investigated 41 bursts occurring during the 850–861 s interval. They estimated that over 1000 bursts occurred over the entire flight, with durations from 20 to 250 ms, amplitudes ranging from a few mV/m to nearly 1 V/m, and with modulation frequencies ranging from less than 1 kHz to over 50 kHz.

The period from 690 to 780 s, outlined in white in Figure 4.2a, showed strong activity on both HF electric-field instruments. This period is expanded in Figure 4.2b for the HFE, and Figure 4.2c from the TAEFWD Z' channel. This channel (and its counterpart Y') is a composite channel derived by taking a linear combination of the real TAEFWD Y and Z channels, such that Z' is parallel to the spin axis (and thus the HFE boom), and Y' is orthogonal to Z' and X. The TAEFWD is somewhat less sensitive than the HFE, and suffers from some instrumental interference which produces the horizontal bands in Figure 4.2c. Nevertheless, after eliminating weak bursts which were dominated by interference or showed no clear modulation, approximately 50 clean TAEFWD snapshots with examples of bursty Langmuir waves were identified in this time period.

Figure 4.3 shows four selected 3-channel, 2048-sample, 0.256 ms TAEFWD snapshots corresponding to the times indicated by arrows in Figure 4.2c. In each example, the top, middle, and bottom panels show the X, Y', and Z' components of the HF electric field, respectively. In all of the waveforms in Figure 4.3, interference appears as discontinuous pulses at approximately 25 μs intervals; however, for the selected snapshots, the wave amplitude is high enough that these interference spikes do not affect identification of peaks and nulls in the wave modulation. All channels were normalized such that the Z' component derived from TAEFWD data was equal in magnitude to the axial component of the HF electric field derived from HFE data, which was in turn converted to absolute electric-field units using pre-launch HFE calibrations, with an adjustment factor to account for probe–plasma sheath capacitance.

Figure 4.3a shows waveforms from within a typical burst of cusp Langmuir waves, occurring at 699.8523 s. The variations in amplitude represent the Langmuir wave modulation which has been studied by many authors (*Bonnell et al.* 1997; *Stasiewicz et al.* 1996; *LaBelle et al.* 2010). The typical modulation frequency is 10 kHz, or 0.1 ms, so the 0.256 ms duration

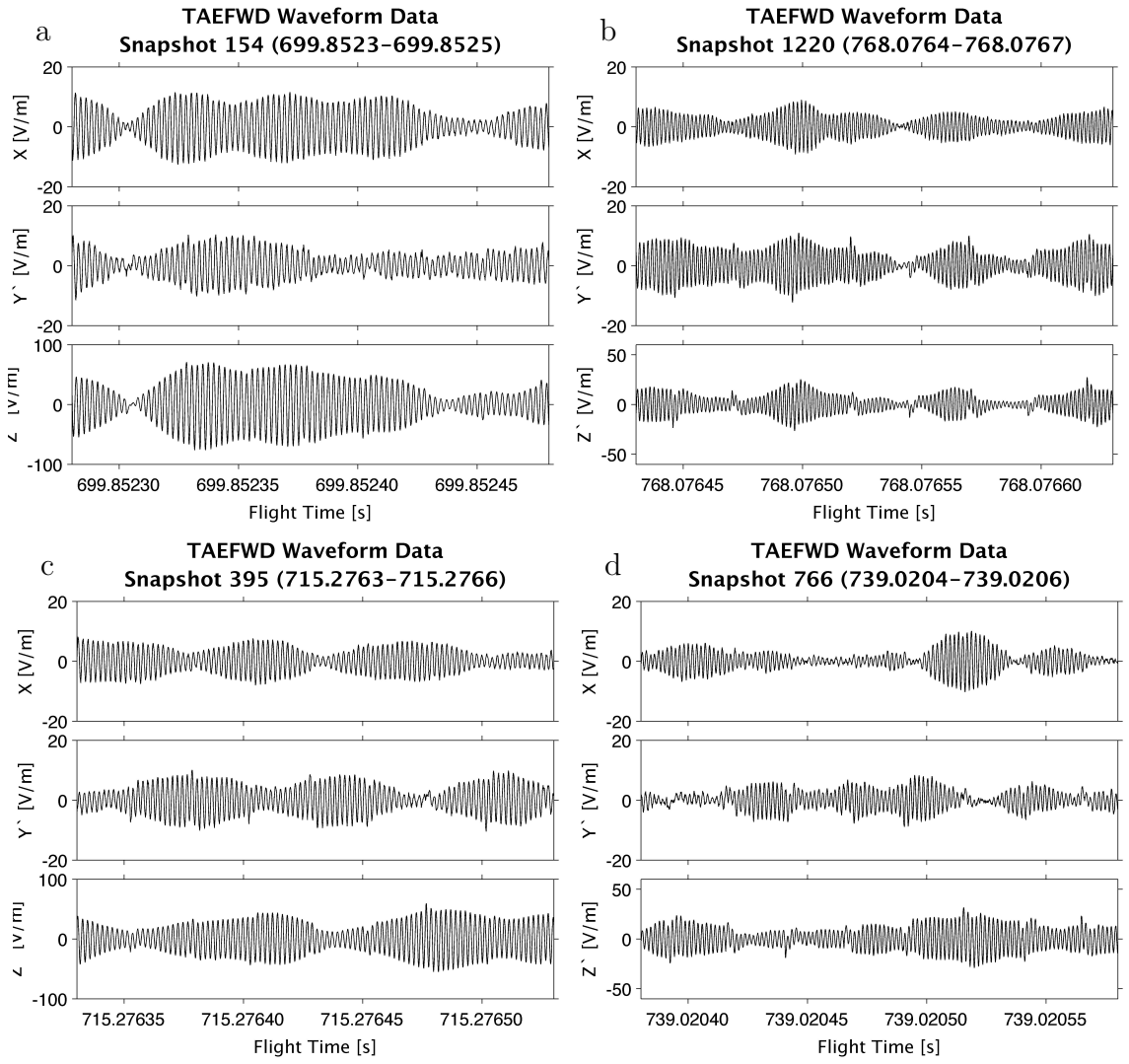

Figure 4.3: Waveform snapshots measured by the TAEFWD, for the four example Langmuir wave bursts indicated by arrows in Figure 4.2c. In **a** and **b**, the modulations of the mutually orthogonal components of wave electric field are synchronous. In **c** and **d** the modulation are not synchronous, indicating anisotropy.

TAEFWD snapshots catch only a small portion of the total modulated wave burst, implying that these plots show only one or a few modulation cycles out of many that occurred. In this example, the modulation nulls about 30 μs from the start of the snapshot are synchronous across all channels, i.e. the modulation of the x, y, and z components of the electric field are in-phase, and the burst modulation is relatively low-frequency ($\sim$ 15 kHz) and approximately monochromatic, implying sinusoidal modulation. Figure 4.3b from 768.0764 s shows an example with faster, multi-frequency modulation. This results in multiple nulls and peaks, which are variably spaced in time. As in the first example, the modulation is isotropic, i.e. in-phase on the three components of the wave electric field.

Of the snapshots with clear, high-powered bursts, up to 25% show modulation that appears to be anisotropic, i.e., the modulation nulls and peaks are not synchronous in the three electric-field components. Figure 4.3c from 715.2763 s shows an example of this behavior, with the modulation nulls and peaks coming at different times in different channels: e.g. a null appears in the X component at 715.276375 s, then in the Y' component 20 μs later, and finally in the Z' component after another 20 μs. In this case, the modulation appears similar in the three electric field components, but peaks and nulls are delayed. In other cases, the modulation of the wave electric field components is not only asynchronous, but the modulation appears entirely uncorrelated. Figure 4.3d shows an example of this behavior, from 739.0204 s. Starting from 739.02000 s, the nulls in this snapshot appear at 45 μs, 49.5 μs, 48.5 μs, and 58 μs in the X component, while the only clear nulls in the Y' component are at 39.5 μs and 52.5 μs, and the Z' component shows no clear nulls.

4.4 Wave Beating and Polarization

These first three-dimensional Langmuir-wave observations from a rocket show that, up to 25% of the time, the modulation of bursty Langmuir waves is anisotropic, meaning that the nulls and peaks are out of phase in the three electric field components. The superposition of two or more linearly polarized waves cannot produce such an effect. We postulate that the anisotropic modulations observed in TRICE high-flyer TAEFWD data result from mixing of Langmuir/whistler-mode waves with a variety of polarizations. To test the plausibility of this postulate, we model the superposition of combinations of wave normal modes which occur in a plasma similar to that encountered by the TRICE high-flyer from 690 to 780 s.

Figure 4.4 shows the result of numerical calculations of wave dispersion characteristics for high-frequency waves in the ionosphere. This dispersion surface was calculated using J-WHAMP, a Java-enhanced version of the Waves in Homogeneous Anisotropic Multicomponent Plasmas (WHAMP) program developed by *Rönnmark* (1982). This code uses numerical approximations of linear Vlasov theory to map out dispersion relations for a given set of plasma and environmental parameters, returning the basic characteristics of the normal modes, such as frequency (ω), wavenumber parallel to the ambient magnetic field ($k_{\|}$), and wavenumber perpendicular to B ($k_{\perp}$). It also returns many additional plasma, wave, and field characteristics, such as Alfvén speed, polarization, Stokes parameters, etc.

The plotted surface in Figure 4.4 is the locus of frequencies and wave vectors corresponding

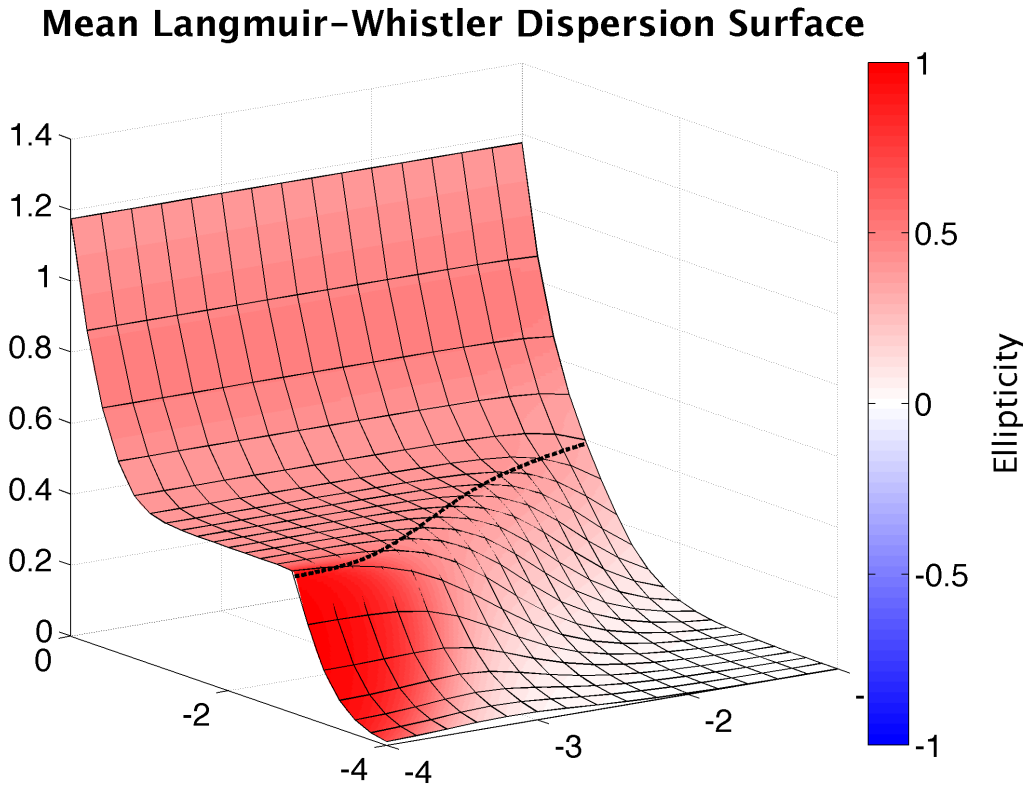

Figure 4.4: A dispersion relation for Langmuir and whistler waves in a homogeneous, magnetized plasma, calculated using the J-WHAMP numerical code. The surface shows frequency normalized to ω_{ce} vs. parallel and perpendicular wavevector (log scales). The model plasma approximately matches the conditions encountered by the TRICE high-flyer from 690 to 780 s. Shading of the surface represents the ellipticity of the modes, which range from left elliptically polarized (blue, not present on this surface) through linear (white) to right elliptically polarized (red). The dashed line is a example contour of constant frequency.

to the normal modes of the plasma. The x and y axes represent the logarithm of $k_\perp$ and $k_\parallel$, respectively, with each normalized to the electron gyroradius ρ_e. The vertical axis shows ω at a given ($k_\perp$, $k_\parallel$), normalized to the electron cyclotron frequency. The dashed line shows a constant-frequency contour, just below f_{pe}. The parameters used to generate this surface were selected to match plasma conditions encountered by the TRICE high-flyer during the 690 to 780 s period: $B_0 = 36.850$ μT (implying $f_{ce} = 1031.800$ kHz), and a single particle species set for electron parameters, with $n = 2149$ cm^{-3} (implying $f_{pe} = 417$ kHz) and an isotropic temperature of 2 eV with no loss cone. The model plasma includes only thermal (background ionosphere) electrons, because this population is what determines the real part of the wave dispersion relation, i.e. the frequencies, wave vectors, and polarization of the normal modes. At these frequencies, ions are a static background, with no significant effect. A more-complex electron beam model would be required to calculate the imaginary part of the dispersion relation (e.g. to examine damping rates), but is not required for our investigation of interference as a function of wave polarization, as an unrealistically high-density beam would be required to affect the mode structure and polarization. In the aurora, beam densities are typically 10^{-3} smaller than the ambient electron density. The significant J-WHAMP outputs for this analysis are those related to the polarization of normal modes: electric-field coefficients for generated waves, and the ellipticity parameter, which is a measure of polarization ranging from -1 (left-circularly polarized) through 0 (linearly polarized) to +1 (right-circularly polarized). In Figure 4.4, the ellipticity is represented by the color of the dispersion surface.

The dispersion characteristics of Figure 4.4 are similar to those calculated by *André* (1985), specifically his 'model 2' for an $f_{pe} < f_{ce}$ regime. In the limit $k_\parallel \gtrsim k_\perp$ and $k_\parallel \rho_e >> 0.001$, the surface corresponds to Langmuir waves, for which $\omega \approx \omega_{pe}$ at intermediate k. Dispersion sets in at short wavelengths ($k_\parallel \rho_e > 0.1$) due to finite electron temperature effects. For $k_\parallel >> k_\perp$ and long wavelengths in the $f_{pe} < f_{ce}$ regime, the Langmuir mode smoothly couples to the whistler mode, and the surface is better described as 'Langmuir-whistler modes' (*Layden et al.* 2011). These mode identifications can also be confirmed by the ellipticity: a region of strong right-elliptical polarization (REP) coincides with the whistler modes, while the Langmuir wave modes are more linearly polarized (LP).

The observations show modulated Langmuir waves which have been interpreted as wave beating due to the presence of multiple normal modes with closely spaced frequencies, e.g. waves near the 500 kHz plasma frequency with frequency separations of approximately 10 kHz. To investigate the intermodulation of such closely spaced normal modes, we can select normal modes from the Figure 4.4 data: one on a specific frequency contour and one near that contour (though not necessarily near the first point), representing waves with relatively similar frequencies. As shown by the dashed line in Figure 4.4, two modes thus selected can have very close frequencies, but significantly different wave vectors and polarizations. For example, one wave can be partway down the whistler dispersion curve, in the range of REP wave modes, and the other can lie in the mostly LP Langmuir wave region.

In order to simulate the superposition of two waves, we start by extracting five parameters—$k_\perp$, $k_\parallel$, and the complex E_x, E_y, and E_z coefficients—from the J-WHAMP output, for two selected normal modes from our dispersion surface. The E coefficients output by J-WHAMP

Table 4.1
WAVE NORMAL MODE PARAMETERS[1].

#	ψ (deg)	LP /REP	f_{pe}/f_{ce}	E (x,y,z)	k $(x/\perp,\ y,\ z/\parallel)$	Ellip
a	45	LP	0.369469	(0.376424, 0.002857i, 0.926443)	(0.003162, 0, 0.007943)	0.3759
		LP	0.366606	(0.391707, 0.003042i, 0.920085)	(0.003236, 0, 0.007762)	0.3732
b	45	REP	0.368377	(0.630643, 0.512265i, 0.582988)	(0.000158, 0, 0.001380)	0.9093
		REP	0.369478	(0.632961, 0.524797i, 0.569165)	(0.000148, 0, 0.001380)	0.9176
c	45	LP	0.369469	(0.376424, 0.002857i, 0.926443)	(0.003162, 0, 0.007943)	0.3759
		REP	0.368377	(0.630642, 0.512265i, 0.582988)	(0.000158, 0, 0.001380)	0.9093
d	45	LP	0.366606	(0.391707, 0.003042i, 0.920085)	(0.003236, 0, 0.007762)	0.3732
		REP	0.369478	(0.632961, 0.524797i, 0.569165)	(0.000148, 0, 0.001380)	0.9176

[1] Determined from J-WHAMP, and used for the waveform simulations shown in Figure 4.5, along with the ellipticity for each mode. Model c uses the first waves from model a and model b, and models c and d differ only in the coordinate system rotation parameter ψ.

are normalized such that $|E| = 1$ mV/m, thus assuring that the interacting waves have comparable amplitudes, and modulation peaks and nulls should be at their most-pronounced. The parameters are plugged into the general plane wave equation summed over both waves

$$\vec{E}(t) = \begin{cases} \left(E_{x1}e^{-\mathbf{i}(k_1\cdot\vec{x}-\omega t)} + E_{x2}e^{-\mathbf{i}(k_2\cdot\vec{x}-\omega t)}\right)\hat{x} + \\ \left(E_{y1}e^{-\mathbf{i}(k_1\cdot\vec{x}-\omega t)} + E_{y2}e^{-\mathbf{i}(k_2\cdot\vec{x}-\omega t)}\right)\hat{y} + \\ \left(E_{z1}e^{-\mathbf{i}(k_1\cdot\vec{x}-\omega t)} + E_{z2}e^{-\mathbf{i}(k_2\cdot\vec{x}-\omega t)}\right)\hat{z} \end{cases} .$$

There exists an ambiguity in any dispersion solution which results in a rotational freedom around the $k_\parallel$ axis. J-WHAMP defines that $k_\parallel \equiv k_z$ and $k_\perp \equiv k_x$, implying that k_y must be zero—this is not a fully general solution. Section 4.5 examines this $k_\perp$ ambiguity with respect to J-WHAMP output, and finds that rotations around the z axis can generate some beat modulation anisotropy, but cannot fully explain the observations. Furthermore, in order to optimally pick up beating between the x and y components of waves, one must rotate all beating waves by an angle $\phi = 45$ degrees around the z axis. Figure 4.5 shows the results of the simulations, for four pairs of normal modes from the Langmuir plane, with $\phi = 45$ degrees. Using J-WHAMP definitions of the coordinates, the x, y, and z directions roughly correspond to those in the TAEFWD data, with z parallel to B_0, and x and y perpendicular. Table 4.1 lists the full parameters (f_{pe}, E, k, and ψ) used for the Figure 4.5 simulations.

Figure 4.5a shows the result of combining two simulated wave modes from the LP Langmuir dispersion region, at sufficiently short wavelengths for $\omega \sim \omega_{pe}$. As expected, the resulting modulation occurs with a 330 μs period ($1/\Delta f => 1/(3$ kHz)). In this case, corresponding to beating of two LP waves, the wave modulation is isotropic, i.e. maxima and minima coincide in time, similar to the observations shown in Figure 4.3a and b. Figure 4.5b shows the similar wave modulation that results from superposing two REP waves selected from the region $k_\parallel \sim 0.001$ and $k_\perp < 0.001$, which is within the whistler-mode part of the dispersion surface. The resulting modulation has a 660 μs period, and shows isotropic modulation.

In Figure 4.5c and d, the wave modes pairs from a and b were combined to make two mixed pairs in order to investigate beating between waves of different polarizations. This combination of one wave mode from each dispersion region yields modulation anisotropy, such that the nulls in each component occur at different times. In Figure 4.5c, the null in the x component is delayed 100 μs from the null in z, and 200 μs from the null in y. This is qualitatively and quantitatively similar to the effect observed in Figure 4.3c.

A close examination of power spectra of the four waveform snapshots shown in Figure 4.3 lends some support to this interpretation; however, for TRICE TAEFWD data, the frequency resolution of the spectra is limited due to the short duration of the waveform snapshots. Figure 4.6 shows power spectra with the horizontal axis zoomed in to a narrow range of frequencies centered around f_{pe} for a given snapshot. The dashed, black line shows power in the (Z') component, which is roughly parallel to B_0, while the red line shows 'perpendicular power', which is the sum of the power in the X and Y' components. As expected, more power is generally found in the parallel direction, but anywhere from 5% to 50% of the power near f_{pe} can be found in the perpendicular direction, depending on snapshot. This implies that a significant fraction of the waves present lie in the oblique regions of k-space (i.e. away

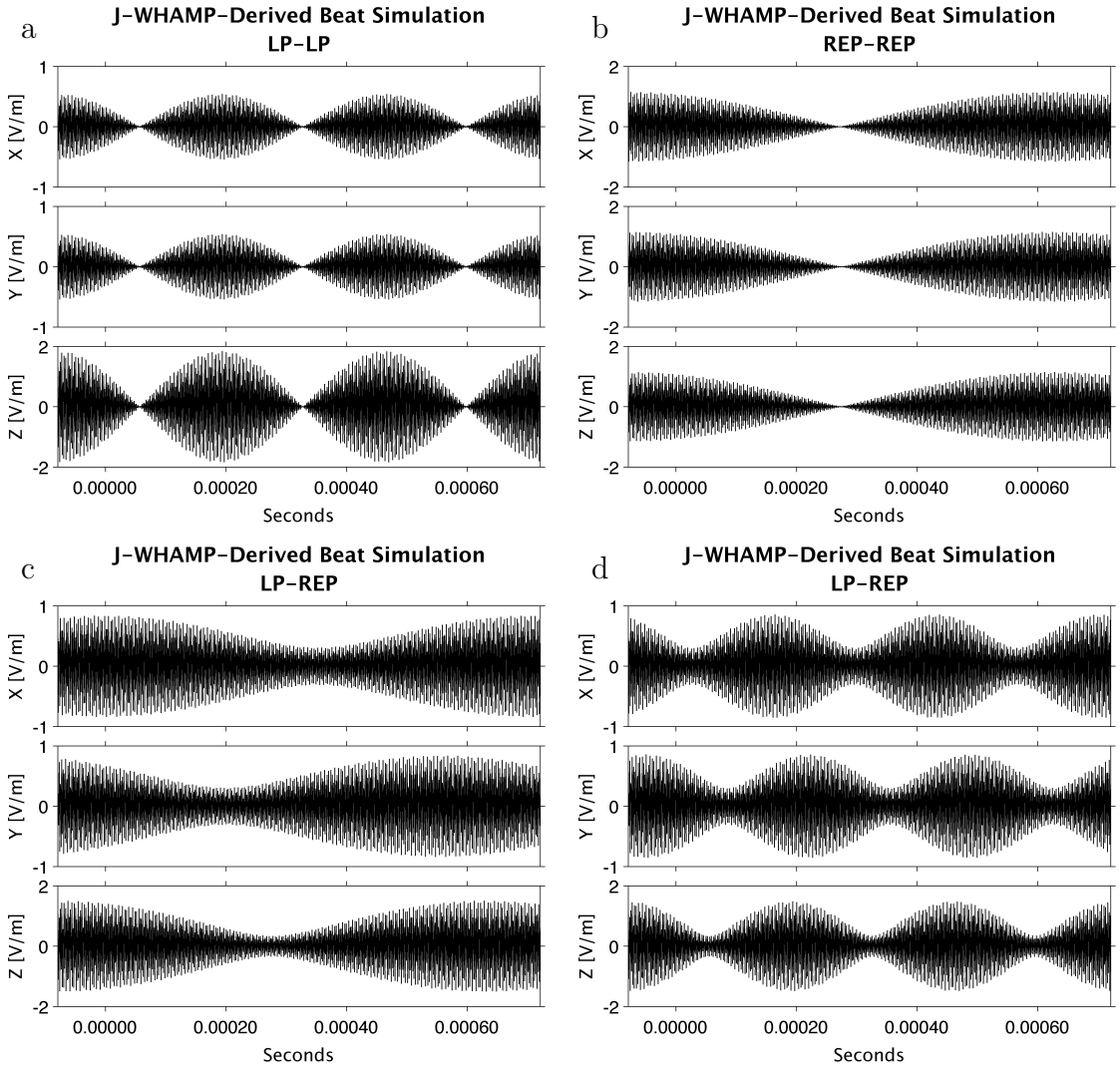

Figure 4.5: Simulations of beating between pairs of waves corresponding to Langmuir-whistler modes calculated with J-WHAMP. In **a** and **b** the simulated beating wave modes have the same polarization, both linearly polarized (**a**) or both right-elliptically polarized (**b**). In **c** and **d** one wave mode is used from the set in **a**, and one from **b**, so the simulated waves have different polarizations, one more-linear, one more-elliptical. **a** and **b** result in isotropic modulation of the three field components, whereas **c** and **d** result in anisotropies. Note that all waves have been rotated through 45 degrees so that J-WHAMP-calculated mode beating will be optimally detected (see Section 4.5).

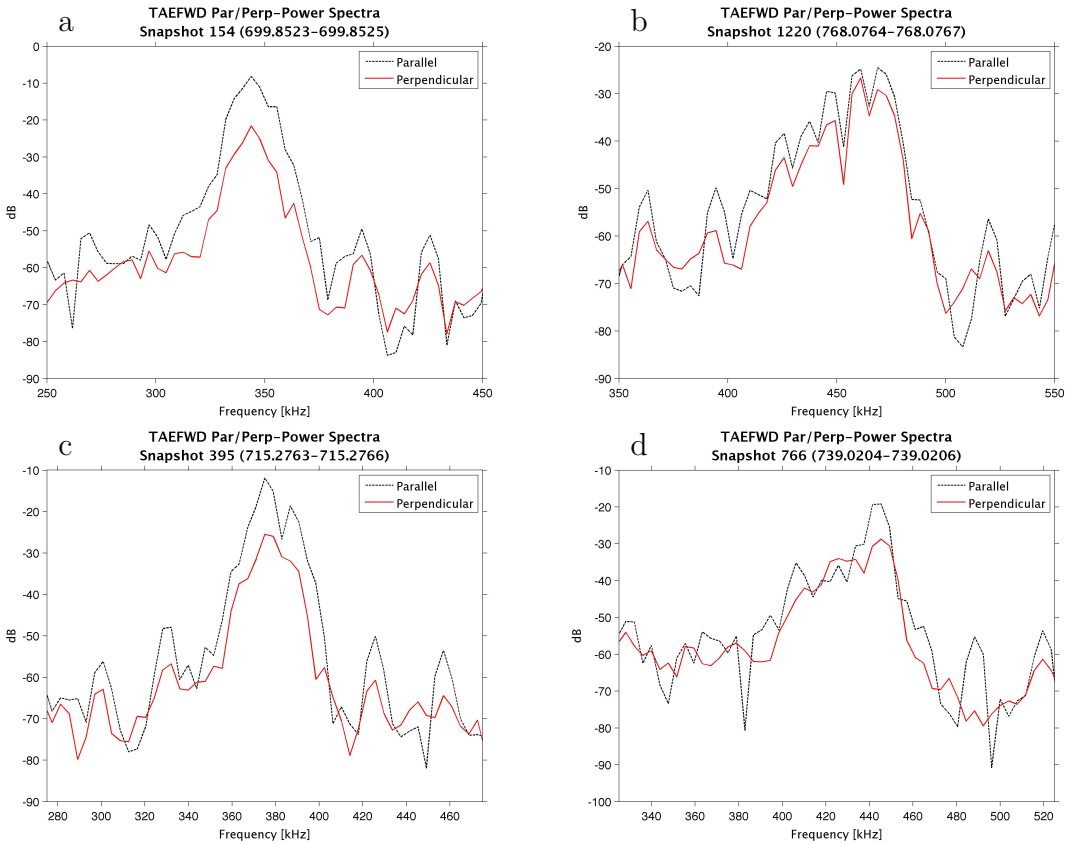

Figure 4.6: Power spectra of the TAEFWD waveform snapshots shown in Figure 4.3, showing power in the parallel (Z') and perpendicular ($X + Y'$) components. The horizontal axis shows a 200 kHz band centered on f_{pe} for the given snapshot. The significant power in the perpendicular direction implies that wave modes from a wide region of k-space are present.

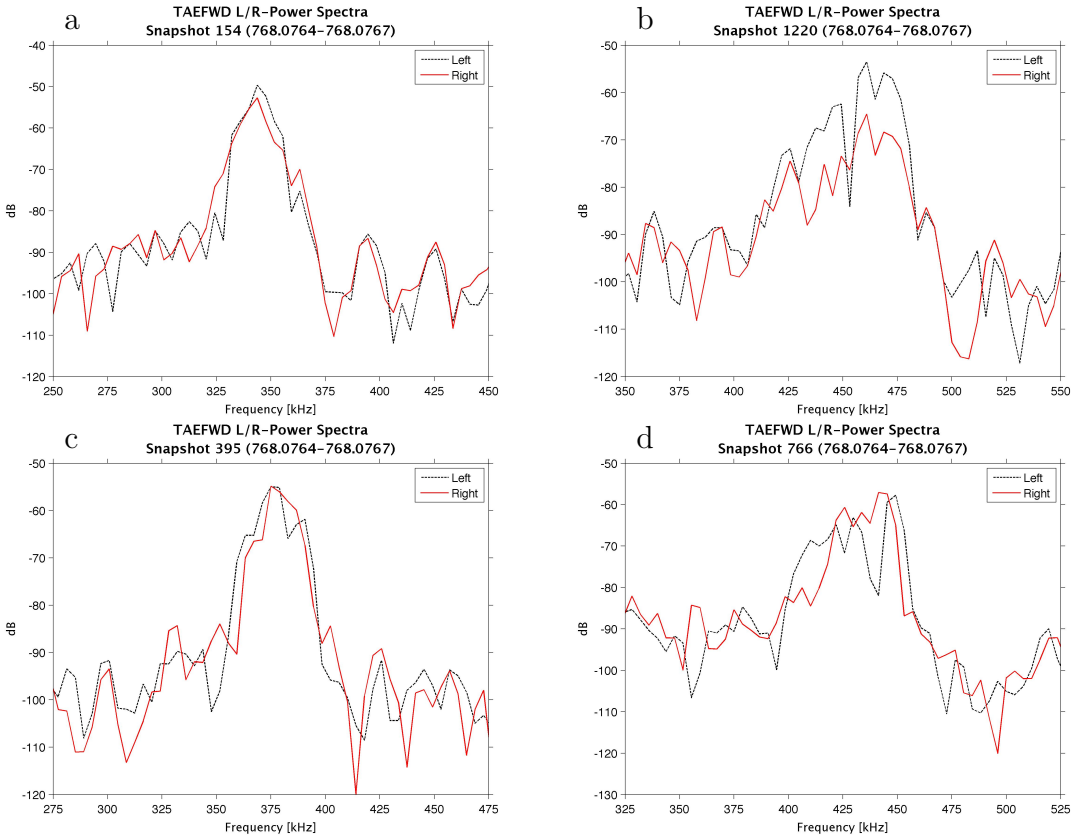

Figure 4.7: Power spectra of the TAEFWD waveform snapshots shown in Figure 4.3, with complex Fourier transforms of the transverse components (X and Y') recombined to estimate the degree of right and left circular polarization, as done in *Kodera et al.* (1977) and *LaBelle et al.* (2010). The horizontal axis shows a 200 kHz band centered on f_{pe} for the given snapshot. While the snapshots are too short to resolve the mode composition in detail, **b**, **c**, and **d** show hints that both linear and elliptical polarizations contribute to the wave modes measured near the Langmuir frequency.

from the x and y axes in Figure 4.4), which implies that multiple wave modes with different polarizations may be present.

A method of spectral analysis of polarization is taken from *LaBelle and Treumann* (1992), adapted from *Kodera et al.* (1977). Given time series data corresponding to two perpendicular, transverse components of the wave electric field, as from the measured X and reconstructed Y' components from the TAEFWD, a spectral power can be estimated for left- and right-polarized waves by recombining the complex Fast Fourier Transforms (FFT) of the time series, according to

$$\begin{aligned} FFT_L &= FFT_X + \mathrm{i} FFT_Y, \\ \text{and} \quad FFT_R &= FFT_X - \mathrm{i} FFT_Y. \end{aligned}$$

The relative power ratio $|FFT_L|^2/|FFT_R|^2$ indicates whether the waves at a given frequency are predominately left, right, or linearly polarized. Figure 4.7 shows the results of this

analysis, again zoomed in near f_{pe}. While the small number of samples in each snapshot limit frequency resolution such that the individual peaks for the beating waves are not resolved, the variations seen in these spectra suggest that mixing of linear and elliptically-polarized waves is occurring to some degree.

4.5 The $k_\perp$ Ambiguity

The background magnetic field provides a natural axis in a plasma environment, which motivates a $k_\parallel$ and $k_\perp$ coordinate system, but with rotational freedom around $k_\parallel$; i.e., $k_\perp$ can lie anywhere in a plane perpendicular to the background magnetic field. J-WHAMP resolves this ambiguity by defining $k_\parallel$ to be along the z axis, $k_\perp$ to be along the x axis, and $k_y = 0$. While $\vec{k}$ does not directly affect the simulations because of the simplification that $\vec{x} = \vec{0}$, information on the wave's orientation will be a part of the complex $\vec{E}_0$, and so a more general simulation will have $k_x \neq k_y \neq 0$. One can simulate such a state by rotating one of the component waves in the beat simulations around $\hat{z}$. Looking at a general $\hat{z}$ rotation by an angle ϕ, and assuming $\vec{E}_0 \in \mathbb{R}$ so that a 100% right-circularly-polarized wave will have components $(E_x, \mathfrak{i}E_y, E_z)$,

$$\begin{pmatrix} \cos\phi & -\sin\phi & 0 \\ \sin\phi & \cos\phi & 0 \\ 0 & 0 & 1 \end{pmatrix} \begin{pmatrix} E_x \\ \mathfrak{i}E_y \\ E_z \end{pmatrix} = \begin{pmatrix} E_x\cos\phi - \mathfrak{i}E_y\sin\phi \\ E_x\sin\phi + \mathfrak{i}E_y\cos\phi \\ E_z \end{pmatrix}.$$

Through judicious use of Euler identities, this can be manipulated into the form

$$\left.\begin{pmatrix} \mathfrak{e}^{\mathfrak{i}\phi}\cdot f(E_x, E_y, \phi) \\ \mathfrak{e}^{\mathfrak{i}\phi}\cdot g(E_x, E_y, \phi) \\ E_z \end{pmatrix}\right| (f,g) \in \mathbb{C}\,.$$

This shows that the rotation can be broken down into complex ϕ-dependent amplitudes f and g times an equal phase shift of the x and y components with respect to z. The fact that the x and y modulation phases remain synchronous would imply that not all of the modulation phase anisotropy seen in TAEFWD data can be explained simply by the beating waves having different wavevectors. In Figure 4.8 this is confirmed in simulation, showing the change in beat patterns while rotating one of the component waves. While there is some small shift in the x-y phase alignment, it is insufficient to reproduce, for example, Figure 4.3c, and can probably be attributed to the small difference in ellipticity between the two chosen wave modes.

An additional effect of the J-WHAMP alignment of $k_\perp$ arises because the axes in 'WHAMP-space' are effectively probes in the simulated plasma environment. With the axes aligned with the waves as output by J-WHAMP, the effect is such that any beating caused by interaction between E_x and E_y cannot be seen, as in Figure 4.9 where no modulation is seen in the y component, which is qualitatively similar to the lack of modulation in the z component of Figure 4.3d. As depicted in Figure 4.9, testing of various amounts of rotation of all beating

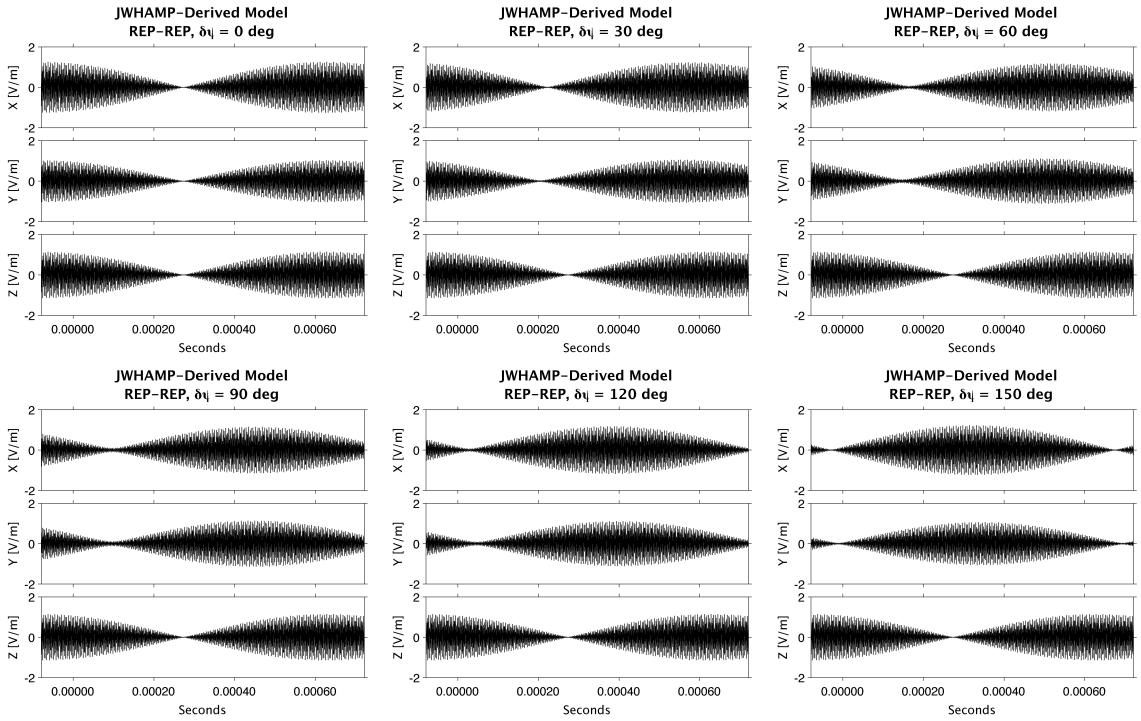

Figure 4.8: Simulation of two beating, mostly-circularly polarized waves, with one held constant and the other rotated through angle ϕ around the z axis. Note that the x and y modulation phases remain mostly aligned.

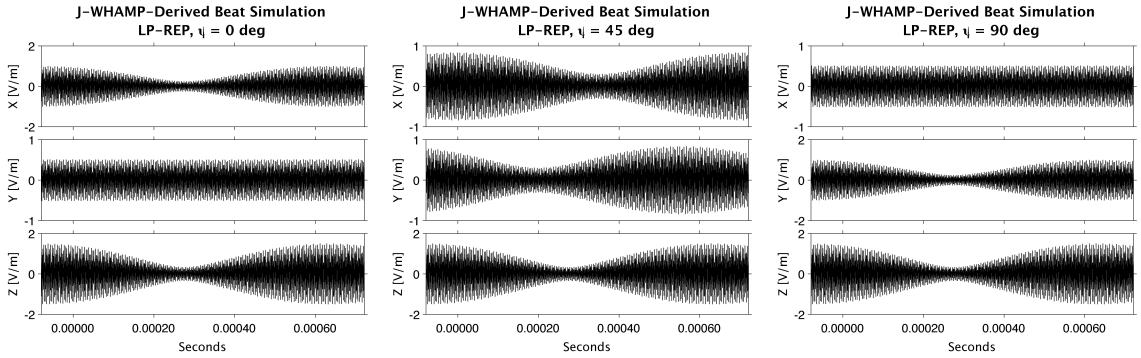

Figure 4.9: Results of rotating the simulation coordinate system through various angles ψ around the z axis, which is essentially the same as changing the orientation of the virtual rocket probes. The original orientation with $\psi = 0$ is entirely insensitive to beating in the y direction. Rotation through $\psi = 90$ degrees causes this insensitivity to move to the x direction, as one would expect with perpendicular axes. Strong beating in all channels with anisotropic modulation phase can be seen with $\psi = 45$ degrees.

component waves around the z axis by an angle ψ (effectively rotating the 'virtual payload' used to 'detect' k and $\vec{E}$), yields the conclusion that the payload orientation can have a significant impact on how well any modulation will be detected, and that $\psi = 45$ degrees is the optimal angle to detect beating in our simulations. It is possible that the physical version of such effects may be seen in the TAEFWD observations, in cases where strong modulations are seen in only two of three directions, e.g. Figure 4.3d.

4.6 Conclusions

An analysis of a period of strong Langmuir waves observed in cusp aurora by two HF electric field instruments on the TRICE high-flyer sounding rocket shows many examples of Langmuir wave bursts modulated at approximately 10 kHz. Previous studies have explained these observations as the result of beating between waves with very close frequencies near the Langmuir cutoff.

The unique 3-D data set provided by the NASA GSFC TAEFWD instrument shows that up to 25% of waveforms selected from the most-intense bursts exhibit anisotropic modulations, i.e. the beat nulls and peaks are not aligned in time across the three perpendicular electric field components. Anisotropic modulation can arise when superposed wave normal modes possess differing polarizations, e.g. if a more linearly-polarized Langmuir wave mixes with a right-elliptically-polarized whistler wave. The J-WHAMP numerical dispersion code shows that conditions appropriate to the observations can produce such waves, and simulations of such superpositions show that they do produce anisotropic modulation. Analysis of wavevector ambiguities (Section 4.5) implies that the orientation of the beating waves with respect to each other and to the instrument probes cannot fully explain the observed effect, though they can mask it. FFT analysis of the 3-D waveform data, though limited due to the

short duration of waveform snapshots, suggests that both linear and elliptically-polarized waves are present near the Langmuir cutoff at these times. Because either proposed origin of the beating waves could produce waves with multiple polarizations, these findings do not resolve the origin of the multiple modes. Nevertheless, these observations illustrate how 3-D measurements can give valuable insight into the nature of wave interactions in the auroral plasma environment, and suggest that future measurements should have a higher duty cycle, and perhaps even be continuous.

Bibliography

André, M., Dispersion surfaces, *Journal of Plasma Physics*, *33*(01), 1–19, doi:10.1017/S0022377800002270, 1985.

Beghin, C., J. L. Rauch, and J. M. Bosqued, Electrostatic plasma waves and hf auroral hiss generated at low altitude, *J. Geophys. Res.*, *94*(A2), 1359–1378, 1981.

Boehm, M. H., Waves and static electric fields in the auroral acceleration region, Ph.D. thesis, University of California, Berkeley, Berkeley, CA, 1987.

Bonnell, J., P. Kintner, J. E. Wahlund, and J. A. Holtet, Modulated langmuir waves: Observations from freja and scifer, *J. Geophys. Res.*, *102*(A8), 1997.

Ergun, R. E., C. W. Carlson, J. P. McFadden, J. H. Clemmons, and M. H. Boehm, Evidence of a transverse langmuir modulational instability in a space plasma, *Geophys. Res. Lett.*, *18*, 1177, 1991.

Gurnett, D. A., J. E. Maggs, D. L. Gallagher, W. S. Kurth, and F. L. Scarf, Parametric interaction and spatial collapse of beam-driven langmuir waves in the solar wind, *J. Geophys. Res.*, *86*(A10), 8833–8841, 1981.

Kaeppler, S., C. A. Kletzing, S. R. Bounds, J. W. Gjerloev, B. J. Anderson, H. Korth, J. W. LaBelle, M. P. Dombrowski, M. Lessard, R. F. Pfaff, D. E. Rowland, S. Jones, and C. J. Heinselman, Current closure in the auroral ionosphere: Results from the auroral current and electrodynamics structure rocket mission, submitted Nov 2011, 2011.

Khotyaintsev, Y., G. Lizunov, and K. Stasiewicz, Langmuir wave structures registered by freja: Analysis and modeling, *Adv. Space Res.*, *28*, 1649, 2001.

Kintner, P. M., J. Bonnell, R. Arnoldy, K. Lynch, C. Pollock, T. Moore, J. Holtet, C. Deehr, H. Steinbaek-Nielsen, R. Smith, and J. Olson, The scifer experiment, *J. Geophys. Res.*, *101*, 1865, 1996.

Kletzing, C. A., J. LaBelle, D. E. Rowland, R. F. Pfaff, S. Kaeppler, and M. P. Dombrowski, Untitled, in process paper on CHARM II WPI data, 2012.

Kodera, K., R. Gendrin, and C. de Villedary, Complex representation of a polarized signal and its application to the analysis of ulf waves, *J. Geophys. Res.*, *82*(7), 1245–1255, 1977.

LaBelle, J., and R. A. Treumann, Poynting vector measurements of electromagnetic ion cyclotron waves in the plasmasphere, *J. Geophys. Res.*, *97 (A9)*(13), 789–797, 1992.

LaBelle, J., I. H. Cairns, and C. A. Kletzing, Electric field statistics and modulation characteristics of bursty langmuir waves observed in the cusp, *J. Geophys. Res.*, *115*(A1), 317, 2010.

Layden, A., I. H. Cairns, P. Robinson, and J. LaBelle, Changes in mode properties versus mode conversion for waves in earth's auroral ionosphere, *J. Geophys. Res.*, *116*(A12328), 2011.

Lizunov, G. V., Y. Khotyaintsev, and K. Stasiewicz, Parametric decay to lower hybrid waves as a source of modulated langmuir waves in the topside ionosphere, *J. Geophys. Res.*, *106*, 24,755, 2001.

Maggs, J. E., Coherent generation of vlf hiss, *J. Geophys. Res.*, *81*, 1707, 1976.

Malaspina, D. M., and R. E. Ergun, Observations of three-dimensional langmuir wave structure, *J. Geophys. Res.*, *113*(A12108), 2008.

McAdams, K. L., J. LaBelle, P. W. Schuck, and P. M. Kintner, Phaze ii observations of lower hybrid burst structures occurring on density gradients, *Geophys. Res. Lett.*, *25*(16), 3091–3094, 1998.

McAdams, K. L., J. LaBelle, and M. L. Trimpi, Rocket observations of banded structure in waves near the langmuir frequency in the auroral ionosphere, *J. Geophys. Res.*, *104*(A12), 28,109–28,122, 1999.

McFadden, J. P., C. W. Carlson, and M. H. Boehm, High-frequency waves generated by auroral electrons, *J. Geophys. Res.*, *91*, 12,079, 1986.

Newman, D., M. Goldman, and R. E. Ergun, Langmuir turbulence in the auroral ionosphere, 2. nonlinear theory and simulations, *J. Geophys. Res.*, *99*, 6377, 1994a.

Newman, D., M. Goldman, R. E. Ergun, and M. H. Boehm, Langmuir turbulence in the auroral ionosphere, 1. linear theory, *J. Geophys. Res.*, *99*, 6367, 1994b.

Rönnmark, K., Whamp- waves in homogeneous, anisotropic multicomponent plasmas, *Tech. Rep. 179*, Kiruna Geophysical Institute, 1982.

Samara, M., and J. LaBelle, Lf/mf whistler mode dispersive signals observed with rocket-borne instruments in the auroral downward current region, *J. Geophys. Res.*, *111*(A09305), 2006.

Samara, M., J. LaBelle, C. A. Kletzing, and S. R. Bounds, Rocket observations of structured upper hybrid waves at fuh = 2fce, *Geophys. Res. Lett.*, *31*(22), 2004.

Stasiewicz, K., B. Holback, V. Krasnoselskikh, M. H. Boehm, R. Boström, and P. M. Kintner, Parametric instabilities of langmuir waves observed by freja, *J. Geophys. Res.*, *101*(21), 515, 1996.